# Less is More: Data-Efficient Adaptation for Controllable Text-to-Video Generation

Shihan Cheng<sup>1</sup> Nilesh Kulkarni<sup>2</sup> David Hyde<sup>1</sup> Dmitriy Smirnov<sup>2</sup>

<sup>1</sup>Vanderbilt University <sup>2</sup>Netflix

{shihan.cheng, david.hyde.1}@vanderbilt.edu {nkulkarni, dimas}@netflix.com

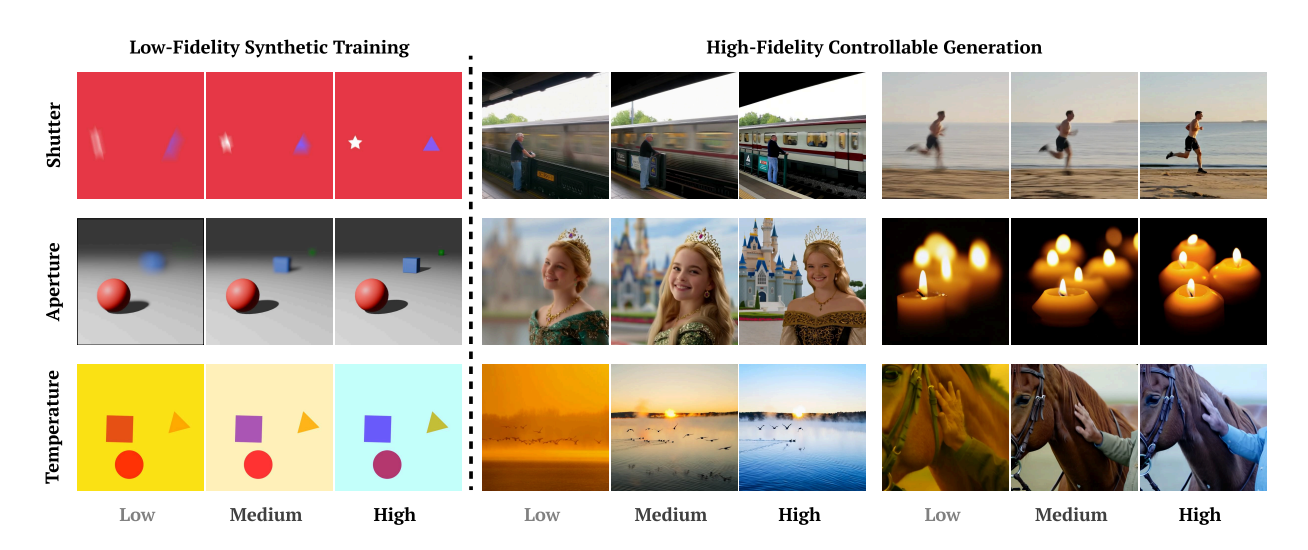


Figure 1. Our "Less is More" framework for data-efficient controllable generation. A T2V backbone, fine-tuned solely on a sparse, low-fidelity synthetic dataset (left), learns to generalize to complex physical controls. This enables precise, high-fidelity manipulation of shutter speed (motion blur), aperture (bokeh), and color temperature during real-world inference (right), driven by a continuous control.

### **Abstract**

Fine-tuning large-scale text-to-video diffusion models to add new generative controls, such as those over physical camera parameters (e.g., shutter speed or aperture), typically requires vast, high-fidelity datasets that are difficult to acquire. In this work, we propose a data-efficient fine-tuning strategy that learns these controls from sparse, low-quality synthetic data. We show that not only does fine-tuning on such simple data enable the desired controls, it actually yields superior results to models fine-tuned on photorealistic "real" data. Beyond demonstrating these results, we provide a framework that justifies this phenomenon both intuitively and quantitatively.

### 1. Introduction

Recent advances in generative AI using diffusion models have enabled unprecedented levels of quality in video generation The primary foundational models for video generation are text-to-video (T2V) such as [28, 43], where users describe their desired creations in natural language. Due to limitations of controllability via text, significant effort has been put into creating methods that accept other input modalities, such as images, keyframes, depth maps, bounding boxes, pose skeletons, driver videos, camera trajectories, and so on [1, 3, 15, 43]. However, achieving consistent, reliable, and intuitive fine-grained control over all aspects of the output video still remains a challenge. In this work, we tackle the problem of adding a control mechanism over specific low-dimensional physical or optical properties, such as camera intrinsics, via a simple synthetic data generation and model fine-tuning framework.

A common pattern that has emerged in methods for producing specialized generative video models is starting with a large "foundation" model, trained on huge amounts of video data, and fine-tuning it on a carefully crafted task-specific smaller dataset [28]. Such datasets help the model

focus on a particular character identity, artistic style, or specialized effect. The success of such approaches hints at the fact that the initial pre-training equips the model with many useful priors implicit in its latent representation, which can be explicitly "coaxed" out during post-training. Our approach is the first approach that aims to enable conditioning on camera effects (like shutter speed, focal length, etc) in pre-trained video generative models for consistent generation. While the quality of the post-training data is indeed critical, we argue and demonstrate that, surprisingly, having data that are perfectly photorealistic and representative of the output domain can not only be unnecessary but even detrimental for certain specializations.

This paper proposes an approach that allows the use of synthetic data to learn several conditioning effects. We contribute a novel joint training approach that factorizes adaptation: a standard low-rank adapter (LoRA) [13] encodes a minimal domain shift, while a disentangled cross-attention adapter learns the conditioning physical effect. Additionally, our paper's contributions include a formal analysis of why this data-efficient approach succeeds. We demonstrate that, counterintuitively, the success of small-data finetuning hinges on the simplicity of the synthetic data. We show that fine-tuning on photorealistic synthetic data, while seemingly a higher-fidelity choice, induces catastrophic forgetting by corrupting the backbone's pre-trained priors, leading to a "content collapse." To quantify this, we introduce a new evaluation framework that measures this generative drift and its impact on semantic fidelity. Using this framework, we show that a model trained on simple data retains its generative diversity and high semantic fidelity, while the model trained on complex data suffers a quantifiable and catastrophic collapse. Our work provides both a data-efficient method for controllable video generation and a formal methodology for diagnosing and preventing backbone corruption during adaptation.

### 2. Related Work

**Text-to-Video Generation.** Diffusion models [12, 36] have become the leading approach for video generation, largely by adapting pre-trained text-to-image models with temporal modules. Early methods like AnimateDiff [10] showed that adding temporal attention to a frozen T2I U-Net [32] enables high-quality motion. The field has since moved toward Diffusion Transformers (DiTs) [26], which underpin state-of-the-art open-source systems such as Hunyuan Video [17] and Wan [43]. Closed-source models including Sora [24], Gen-3 [33], and Kling [38] further push the frontier with long-form, high-fidelity, physically consistent video. Although our experiments use Wan T2V model, our fine-tuning paradigm and evaluation framework are model-agnostic and apply to any video diffusion backbone.

Controllable Generative Models. Recent work introduces explicit control in generative models through spatial conditions such as depth, masks, sketches, boxes, and segmentation maps [2, 4, 18, 42, 44]. ControlNet [55] and T2I-Adapters [22] support such inputs efficiently, with extensions to video focusing on camera pose and trajectory [11, 45, 51]. Methods like Bokeh Diffusion [7] and Generative Photography [53] model physical imaging effects, but their image-based designs fail to generalize to video due to temporal inconsistency. Token-based conditioning via CSaT [6] offers implicit control but remains data-heavy. Large-scale, richly annotated video datasets for physical camera parameters are challenging to obtain. Image LoRAs [13] provide lightweight adaptation for effects including motion blur, bokeh, restoration, and superresolution [7, 25, 37, 56]. Our approach builds on these ideas by injecting scalar physical parameters through a decoupled cross-attention adapter for controllable video synthesis, enabled by targeted synthetic data.

Learning from Synthetic and Sparse Data. The difficulty of large-scale video collection has led to work showing that strong representations can emerge from simple synthetic data [21, 39]. Procedurally generated videos can rival natural-video pretraining [52], and synthetic datasets often serve as effective substitutes for real videos [9, 16]. Synthetic 3D environments also provide precise labels for tasks like optical flow, tracking, and video depth [5, 48, 57], and recent methods use such data for low-shot motion learning [31, 47]. These results suggest that motion priors need not rely on complex natural data, motivating our use of sparse, task-specific synthetic supervision to condition T2V models on camera parameters such as shutter speed, aperture, and temperature.

Evaluation and Metrics for Generative Video Existing one-shot fine-tuning methods [46] and even zero-shot approaches [8, 29, 49] still struggle to generate high-quality, varied videos. Even just quantitatively evaluating and comparing against such such models remains a complex, multidimensional problem. Common metrics include the Fréchet Video Distance (FVD) [40, 41], which measures distributional similarity in a learned feature space for action recognition, and CLIP Score [30], which quantifies text-video semantic alignment. More recent works have proposed adaptations for video, such as X-CLIP Score [23], or more robust alternatives like VOA Score [19], which is less prone to error on complex compositional prompts. Shuttleworth et al. [35] further investigate how LoRA and full fine-tuning alter pre-trained diffusion models by analyzing changes in their weight matrices through spectral decomposition. While benchmarks such as VBench [14]—which we adopt in our evaluation—offer a suite of metrics for assessing temporal consistency, object fidelity, and aesthetic quality, we identify a critical methodological gap: standard metrics fail to quantify the intrinsic complexity of the fine-tuning data. We address this with a novel metric as part of our contribution.

### 3. Method

Our primary objective is to introduce direct, lowdimensional, continuous control over a specific attribute of the output produced by a T2V generative model. We achieve this by fine-tuning a pretrained T2V model on a carefully assembled dataset, which exhibits sufficient variation along the desired control axis. In order to make this fine-tuning possible, we introduce two architectural modifications to the base model. Our overall training architecture is illustrated in Figure 2, and the supplementary material contains complete pseudocode for our method. Disentangled Conditioning Module Following recent work in controllable generation [50], we employ a dedicated crossattention module in order to inject the conditioning signal. We normalize the condition (which in our experiments is a scalar value) to obtain  $c \in [-1,1]$ . This condition is projected to a higher-dimension embedding vector via a small multi-layer perceptron (MLP):  $e_{cond} = MLP_{cond}(c)$ . The embedded conditional signal  $e_{cond}$  is then injected into the model using a dedicated cross-attention mechanism that operates in parallel with the main text cross-attention. We insert this conditional cross-attention adapter into the deepest third of the original model's transformer blocks. For a given query q from the video latent, the output of the cross-attention block is a linear combination of the text-conditioning  $y_{\text{text}}$  and the attribute-conditioning  $y_{\text{cond}}$ . Backbone LoRA Rather than attempting to construct a dataset for fine-tuning that uniformly and consistently exhibits variation along the desired control axis and matches the natural video distribution of the original T2V model, we make the deliberate choice to construct datasets that satisfy only the former requirement. This decision frees us from having to do careful curation of natural videos or difficult photorealistic rendering but rather allows us to focus on creating simplistic synthetic examples that illustrate the conditioning effect. However, fine-tuning on such out-of-domain datasets inevitably induces content drift. To address this, we employ a joint training strategy where a backbone LoRA is optimized alongside the conditioning module. This approach enforces a "separation of concerns": the backbone LoRA absorbs the synthetic domain shift, allowing the conditional adapter to focus exclusively on disentangling the physical control signal. Critically, at inference time, we revert this drift by selectively discarding the backbone LoRA weights from all blocks that are not equipped with the conditional adapter. This restores the model's original generative priors in the majority of the network while preserving the learned control mechanism.

### 4. Dataset Construction

We evaluate our method on three scalar camera parameters—shutter speed, aperture, and color temperature—using synthetic datasets that isolate their respective effects: motion blur, depth of field, and color tone. We adopt a simple, non-photorealistic domain to enable precise procedural control and clean variations along each conditioning axis. To ensure diversity within this controlled setting, we apply two forms of scene randomization.

Control Scalar Randomization. The primary driver of generalization in our method is the low-dimensional adapter (Sec. 3). To complement this and ensure a continuous response, we employ a multi-level stratified sampling strategy rather than relying on fixed discrete values. We partition the normalized range [-1,1] into N equal-width bins and sample uniformly from within each bin, applying this strategy across several hierarchical layers. This "pyramid" approach ensures that our sparse dataset provides a rich, continuous signal by concentrating sampling density near the center of the control space, preventing overfitting to specific values.

Scene Content Randomization. We design a dataset of geometric primitives that balances semantic simplicity with functional expressiveness, avoiding the confounding complexity of photorealistic data. Each training scene is procedurally generated with a randomized composition of moving shapes. This configuration ensures that the necessary conditions for physical control are visually observable—such as varying trajectories for motion blur or overlapping depth planes for aperture—while eliminating unnecessary semantic details that could induce backbone corruption.

**Photorealistic Ablation Dataset.** To test our "Less is More" hypothesis, we conduct a controlled ablation comparing data content. We construct a high-fidelity "photorealistic" dataset and a "simple synthetic" counterpart. Each dataset consists of only one scene per physical effect, thereby isolating data complexity as the sole experimental variable. The photorealistic scenes, characterized by high semantic complexity, are as follows:

- **Shutter Speed:** We simulate motion blur by applying temporal averaging (frame accumulation) to clips from a high-speed (240-fps) video of a dynamic scene.
- **Aperture:** We generate depth-of-field variations by applying BokehMe [27] to a single image featuring a complex foreground subject and detailed background.
- Color Temperature: We generate color variations by applying a physics-based Kelvin transformation to a single natural outdoor scene with a broad color palette.

This dataset is used in our experiments (Sec. 6) to demonstrate the risks of backbone corruption.

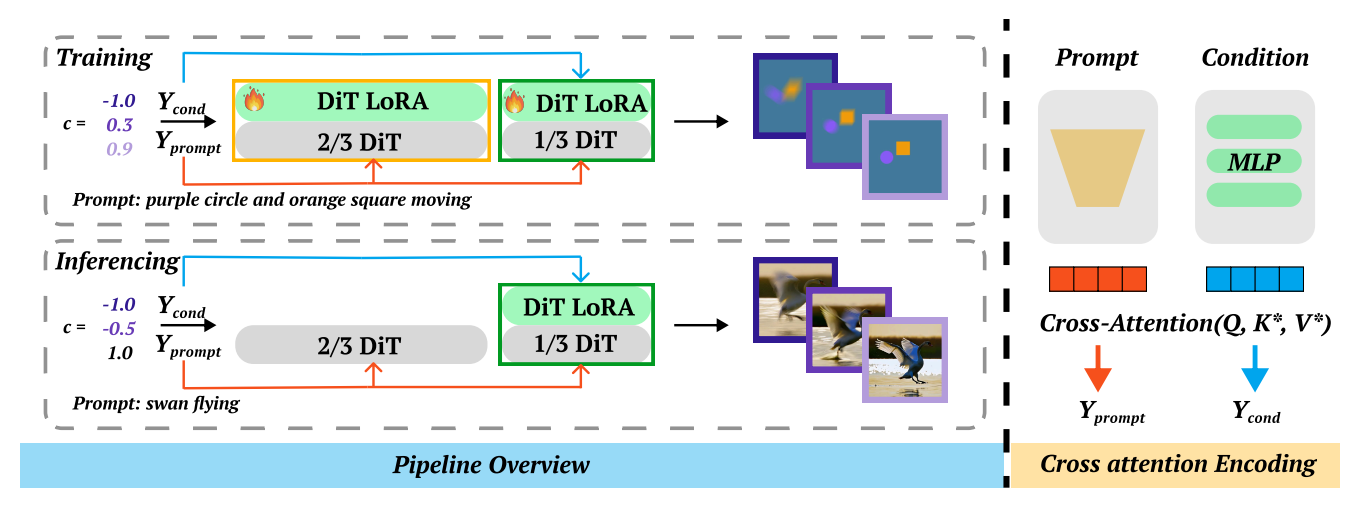


Figure 2. Overview of our controllable generation pipeline. To achieve decoupled control, we encode the scalar condition separately from the text guidance via a parallel cross-attention module. During training (top), we optimize the conditional adapter while actively updating the backbone by injecting LoRA layers into all DiT blocks. During inference (bottom), we discard the LoRA weights from the shallow two-thirds of the transformer blocks, retaining only the conditional adapter and backbone LoRA in the deepest third of the blocks. This selective retention enables high-fidelity physical control while minimizing semantic corruption of the backbone.

### 5. Evaluation Methodology

We propose a two-stage evaluation framework to measure the drift and corruption of the model quantitatively. The first stage, our novel Fast Evaluation Protocol (FEP), introduces lightweight metrics to quantify the magnitude and velocity of backbone changes during fine-tuning. The second stage, the Slow Validation Protocol (SVP), employs established, full-scale metrics to assess the final generative quality and temporal coherence, allowing us to interpret the nature of the changes measured by FEP.

### 5.1. Stage 1: Fast Evaluation Protocol (FEP)

The FEP is a computationally efficient protocol designed to quantify the magnitude of semantic and distributional shifts in a fine-tuning model relative to its original state. The protocol consists of a single-step denoising pass to generate a minimal 4-frame output from a fixed latent seed. This pass is repeated across a broad, semantically diverse prompt set, with specific details provided in our experimental setup (Sec. 6).

**FEP Metrics.** We define two metrics that compare the single-step output of an adapted checkpoint against the original (pre-trained) backbone in the CLIP embedding space.

- Single-Step Fidelity (SSF) Score: The average perprompt cosine similarity between the original backbone's and the adapted checkpoint's embeddings. This measures adherence to the original model's semantic priors. A score near 1.0 indicates minimal semantic change, while a low score signifies a major shift.
- Single-Step Fréchet Distance (SS-FD): The Fréchet Distance between the full embedding distributions of the

- original backbone and the adapted checkpoint. This measures holistic distributional divergence. A high score indicates a significant shift in the model's output distribution away from the original.
- Baseline Calculation: To establish a baseline for inherent variance, we compute these metrics by comparing the original T2V backbone against itself, using only different random seeds. This baseline captures minimal, non-deterministic drift. An adapted checkpoint is thus considered to have minimal backbone change if its SSF score and SS-FD score is comparable to this baseline value.

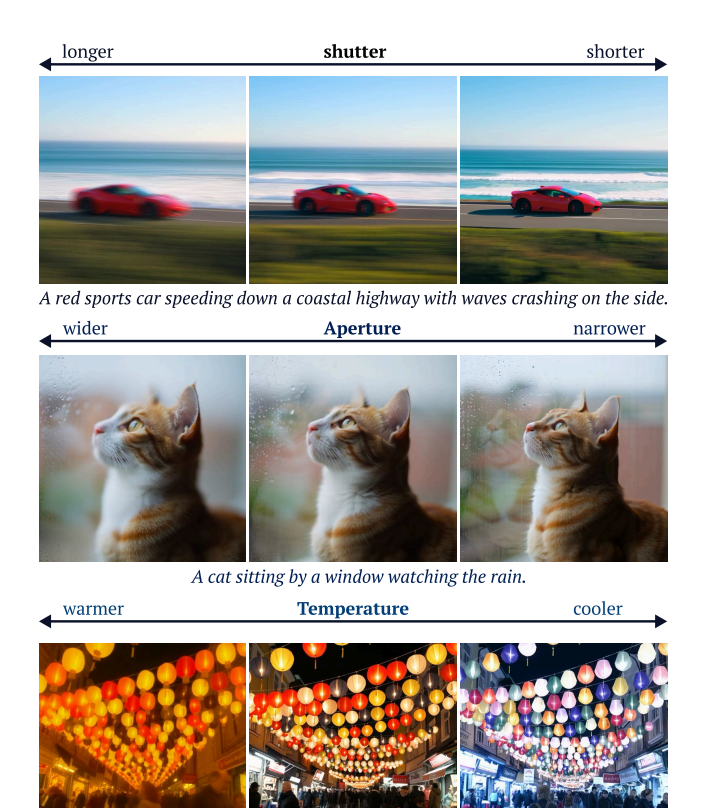
Quantifying Dataset Complexity via Drift Rate. The FEP metrics enable us to quantify dataset complexity by its impact on the model. We define the Distributional Drift Rate  $(\mathcal{V}_{drift})$  as the rate of change in our FEP metrics:  $\mathcal{V}_{drift} = \delta(\text{SS-FD})/\delta(\text{steps})$ . A low-complexity dataset (e.g., our 2D primitives) exhibits a low  $\mathcal{V}_{drift}$ . Conversely, a high-complexity dataset (e.g., photorealistic scenes) induces a high  $\mathcal{V}_{drift}$ . This metric thus provides a quantitative measure of dataset complexity by reflecting the magnitude of change it induces in the backbone.

### **5.2. Stage 2: Slow Validation Protocol (SVP)**

The SVP stage is designed to assess the final generative quality of a model using established, full-scale metrics. It involves a full denoising process to assess both semantic fidelity and perceptual quality.

**SVP Metrics.** We assess two primary categories of metrics:

• Semantic Fidelity (Backbone Health): We compute video-text alignment using the X-CLIP Score [23] and the VQA score [19]. Cross-referencing these scores with the



A bustling night market filled with colorful lanterns and moving crowds.

Figure 3. Qualitative results for Joint Inference. Retaining the full backbone LoRA weights is capable of yielding high-quality generation, supporting the robustness of our data-efficient training.

 $V_{\text{drift}}$  from FEP allows us to diagnose the adaptation: a high-velocity drift is *benign* if final scores are high (successful adaptation), but *malignant* if they collapse (catastrophic forgetting).

• Video Quality & Temporal Coherence: We use six metrics from VBench [54] to evaluate the generated video quality independent of text guidance: subject/background consistency, motion smoothness, dynamic degree, aesthetic quality, and imaging quality.

### 6. Experiments

To validate our "Less is More" hypothesis and analyze how different data strategies impact backbone fidelity, we conduct two primary groups of experiments. We use the WAN 2.1 [43] as our T2V backbone for all fine-tuning and evaluation.

### 6.1. Experimental Design

• Group 1: Data Complexity (Syn vs. Real). To isolate the effect of data content, we conduct a controlled one-shot comparison. For each camera parameter, we train

two models on minimal data: (1) a model trained on a single synthetic scene and (2) a model trained on a single photorealistic scene (per Sec. 4). From each scene, we sample 7 scalar conditions to create the training data. This ablation is evaluated using our FEP on the 800-prompt VBench benchmark [54].

• Group 2: Inference Strategy (Decoupled vs. Joint). To evaluate our proposed inference strategy and also ablation study on, we use our full model trained on the complete pyramid synthetic dataset (Sec. 4) for each camera parameter. Then compare two inference modes: Decoupled ("clean" inference, pruning shallow DiT LoRAs) and Joint ("dirty" inference, retaining all DiT LoRAs). This comparison is evaluated using our SVP on a curated 96-prompt high-motion suite, which involves a full denoising process of 50 steps to generate 49 frames.

### 6.2. Results and Analysis

Our quantitative results are presented in Fig. 4. and Tab. 1.

### 6.2.1. Group 1: Synthetic Data Prevents Forgetting

**Drift Monitoring (FEP):** The results (Fig. 4, Top Row Left) strongly support our "Less is More" hypothesis. The FEP monitoring shows that the model trained on photorealistic "Real" data (dashed line) exhibits a much faster rate of change in its FEP scores per training step compared to the model trained on "Syn" data (solid line). This observation validates that complex, photorealistic data induces a significantly faster and more severe contextual drift in the T2V backbone than our simple, synthetic data.

Corruption Analysis (SVP): The SVP validation (Fig. 4, Top Row Right) confirms the nature of this drift. The "Real" model's semantic scores (X-CLIP, VQA) collapse, indicating malignant, catastrophic forgetting. Conversely, our "Syn" model's scores remain on par with the baseline, proving simple synthetic data is superior for avoiding backbone corruption.

### **6.2.2.** Group 2: Decoupled Inference Retains Fidelity

FEP & SVP Analysis: The results (Fig. 4, Bottom Row Right) validate the superiority of our proposed **Decoupled** ("clean") inference. The FEP analysis shows it barely impacts the backbone, with drift remaining around the baseline. The SVP analysis confirms this, showing minimal semantic corruption (SVP scores change <2%). Meanwhile, the **Joint** ("dirty") inference, while inferior, shows only a slight, acceptable score reduction. This confirms our training is robust and does not cause catastrophic degradation, remaining capable of high-fidelity controllable generation (Fig. 3).

**Video Quality (VBench):** As shown in Tab. 1, a key finding is the stability of the VBench video quality metrics. Both our "clean" and "dirty" inference on model training

Table 1. Quantitative SVP Results. Decoupled ("clean") and Joint ("dirty") inference methods against the baseline using our SVP and
VBench metrics. The evaluation covers all three controls: Shutter (ST), Aperture (AP), and Temperature (TP).

Metric	Baseline	ST(dirty)	ST(clean)	AP (dirty)	AP (clean)	TP (dirty)	TP (clean)
Semantic Fidelity				1			
X-CLIP Score	25.390	25.295	25.587	25.181	25.595	25.487	25.595
VQA Score (Qwen-VL)	0.522	0.453	0.521	0.427	0.513	0.550	0.532
Video Quality				İ		İ	
Subject Consistency	0.951	0.939	0.946	0.968	0.951	0.960	0.950
Background Consistency	0.973	0.963	0.969	0.979	0.973	0.975	0.972
Motion smoothness	0.988	0.983	0.987	0.994	0.987	0.990	0.989
Dynamic Degree	0.427	0.688	0.469	0.219	0.438	0.406	0.417
Aesthetic Quality	0.606	0.576	0.604	0.629	0.610	0.620	0.605
Imaging Quality	0.618	0.531	0.596	0.596	0.633	0.664	0.623

on synthetic dataset maintain scores for Subject Consistency, Background Consistency, Motion Smoothness, and Aesthetic Quality that are nearly identical to the original baseline. This is a crucial result: it demonstrates that our dataset selection and inference design successfully disentangles the new physical control without introducing unwanted artifacts or degrading the backbone's core generative quality, which is a common failure case.

### 6.3. Visual Condition Comparison

Apart from the comparisons via training data and inference methods, we also conducted some qualitative comparisons to prior works such as WAN 2.1 [43], Bokeh Diffusion [7], and [53]. Fig. 5 compares the condition ability of different workflow, text-based prompting in the T2V backbone (WAN 2.1) exhibits significant semantic entanglement. This is particularly evident in the Shutter Speed test (Row 1), where the baseline either struggles to associate shutter speed changes with motion blur, or generates a lower-fidelity scene by creating a "metalic" door instead of the requested glass one. A similar entanglement occurs in the Temperature test (Row 3), where the baseline misinterprets color temperature as weather, incorrectly altering the scene's environment (e.g., adding snow) rather than its color tone. Our method overcomes these shortcomings by correctly applying the physical effect of shutter speed (motion blur) without this semantic or fidelity confusion. Furthermore, for Aperture (Row 2), our model generates high-fidelity bokeh effects comparable to specialized, dataintensive baselines such as Bokeh Diffusion [7] and Generative Photography [53]. These results validate our central hypothesis: our data-efficient synthetic training achieves robust physical disentanglement via a low-rank adapter, eluding the limitations of entangled text prompts and rivaling the quality of data-heavy methods. The supplementary material (see Section F) provides a number of additional examples (as videos) of our method that demonstrate the consistency

of on a range of control values.

### 7. Analysis

Beyond our quantitative metrics (Sec. 5), we develop a suite of data-free analysis techniques. These methods directly analyze the geometric properties of the model's weights and their functional outputs, removing any dependency on specific data samples at test time. To validate our hypotheses on adaptation and disentanglement, we briefly introduce these techniques here and leave the full implementation details in the supplementary material.

# 7.1. Hypothesis 1: Low-Fidelity Data Prevents Catastrophic Forgetting

Our first hypothesis is that fine-tuning on our low-fidelity "synthetic" dataset results in a "cleaner" backbone LoRA update. We posit that this preserves the pre-trained model's general knowledge and avoids the catastrophic forgetting that occurs when training on high-fidelity "real" data.

**Method: Backbone Intruder Dimension Check.** We apply the "intruder dimension" analysis from Shuttleworth et al. [34]. We perform an SVD on the original backbone weight  $W_{pre}$  and its final adapted version  $W_{lora} = W_{pre} + \Delta W_{lora}$ .

An "intruder" is defined as a new, high-ranking singular vector in  $W_{lora}$  that is dissimilar (cosine similarity  $< \epsilon$ ) to all singular vectors in  $W_{pre}$ . A high intruder count is a mathematical signature of catastrophic forgetting; therefore, a low count signifies a successful, non-destructive adaptation to the backbone's existing spectral structure.

The full results of this analysis are shown in the supplementary material (Section E.1). The findings, which compare models trained on different datasets, align perfectly with our conclusions in Sec. 6. This alignment validates both our "Less is More" hypothesis and the effectiveness of our spectral analysis tools.

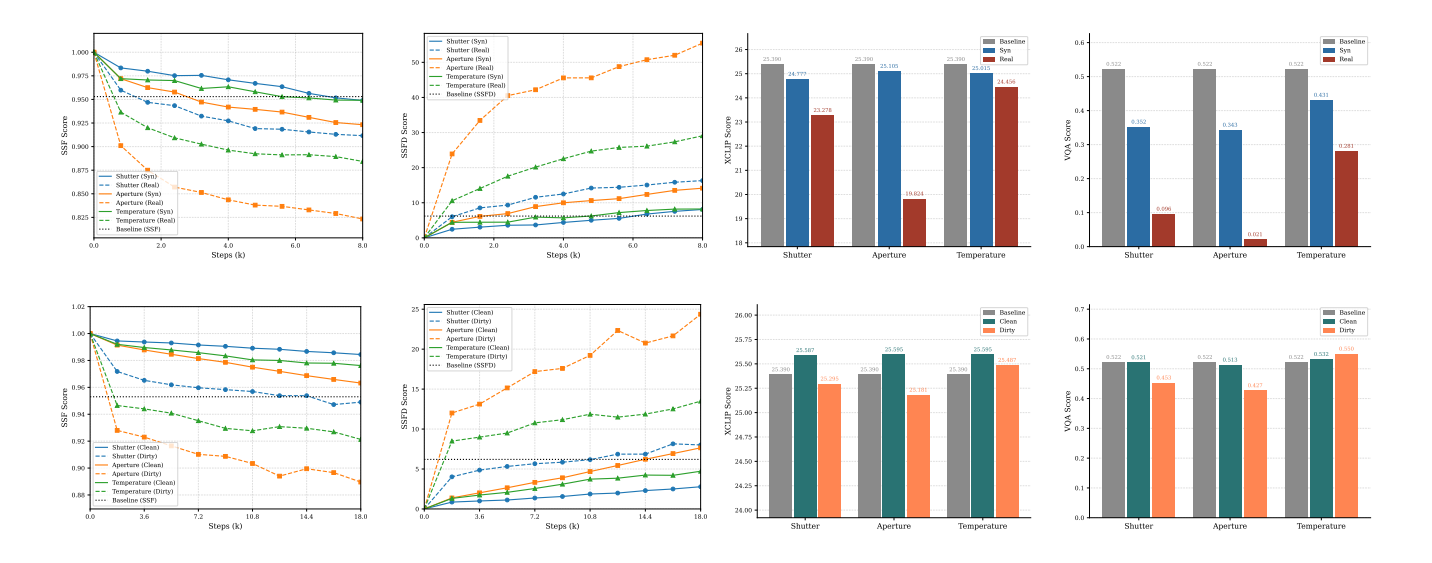


Figure 4. Ablation studies on data complexity and inference strategy. Top Row: Synthetic vs. Real Data. A one-shot comparison of fine-tuning on our low-fidelity synthetic ("Syn") versus complex photorealistic ("Real") data. (Left) FEP monitoring tracks SSF and SS-FD over training steps. (Right) SVP validation bar charts show final X-CLIP and VQA scores. Bottom Row: Decoupled (Clean) vs. Joint (Dirty) Inference. An ablation on our full pyramid-trained model. (Left) FEP monitoring tracks SSF and SS-FD against training steps. (Right) SVP validation bar charts compare final X-CLIP and VQA scores for our proposed "clean" inference and the "dirty" Inference.

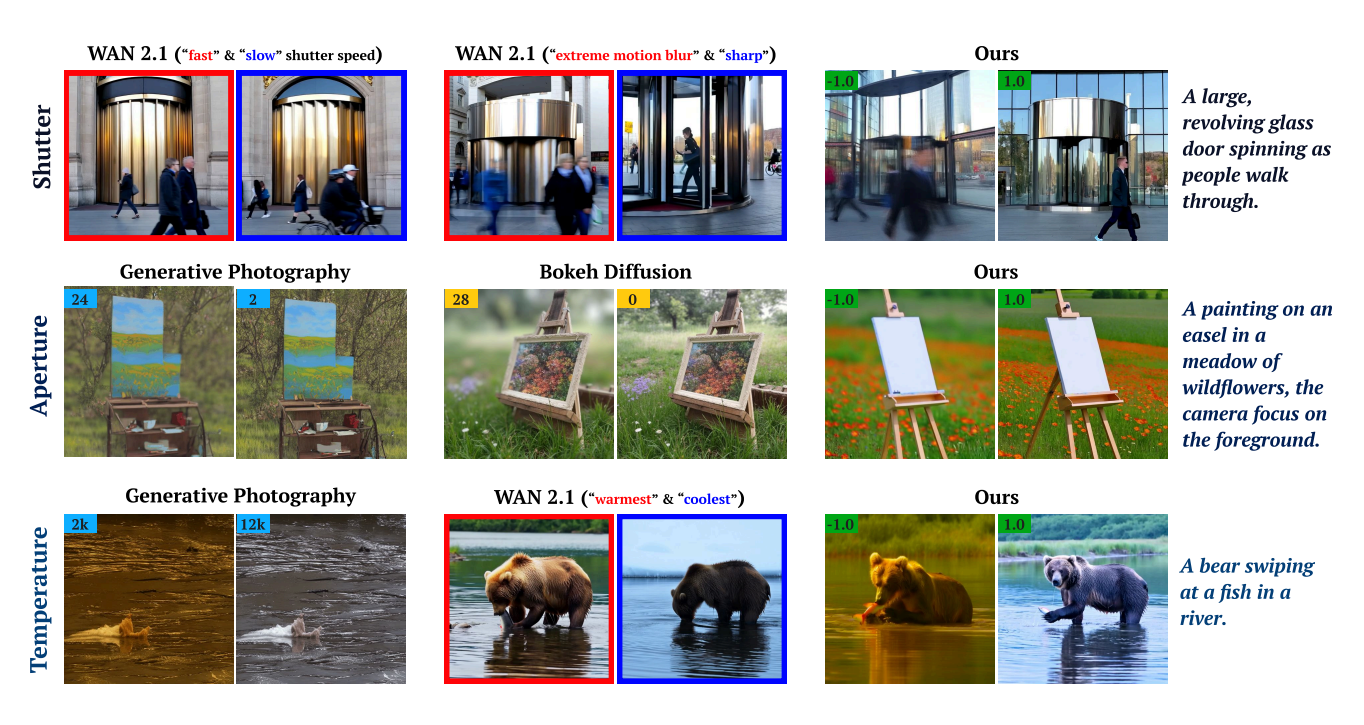


Figure 5. Qualitative comparison of physical controls. We compare our method against text-based prompting in a T2V backbone (WAN 2.1) and specialized, data-intensive image baselines [53] and Bokeh Diffusion [7].

# 7.2. Hypothesis 2: Low-Rank Conditional Representation

Another hypothesis is that the adapter has learned an efficient, compact representation for the physical effect, which is a sign of good generalization.

**Method: Effective Rank Test.** The output of the conditional branch,  $y_{\text{cond}}$ , is a linear combination of the value vectors in  $V_{\text{cond}}(c)$ . We can therefore analyze the dimen-

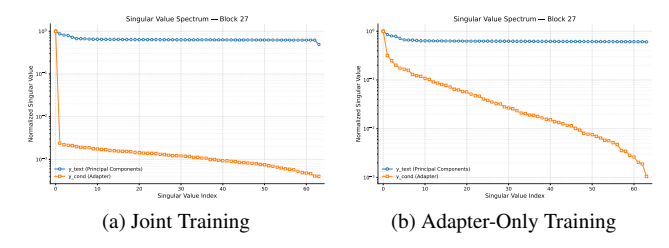


Figure 6. Singular Value Spectrum of the Conditional Signal (y\_cond\_principal) in Block 27. (a) In our jointly trained model, the conditional signal exhibits a sharp spectral decay with an effective rank of 1, proving the model learned an efficient, low-dimensional representation for the pure physical effect. (b) In contrast, for the adapter-only trained model, the signal is high-rank, with a slow spectral decay that mirrors the complexity of the content signal (y\_text). This is definitive evidence that the adapter was forced to memorize the content of the training data.

sionality of this value tensor directly. We generate  $V_{\rm cond}(c)$  for a strong condition (c=1), reshape it into a 2D matrix, and compute its SVD to analyze its singular value spectrum, just as we states in Sec. 3 a successfully factorized model should learn an efficient and compact representation for the conditioning. A physical effect, such as motion blur, should not require a high-dimensional feature space. A low-rank representation is a strong indicator of good generalization, suggesting that the model has learned the "essence" of the effect rather than overfitting to training data artifacts.

### 7.3. Comparative Spectral Analysis of Factorization

To validate our factorization hypothesis, we conduct a comparative spectral analysis on our "Good" (Jointly Trained) checkpoint and a "Bad" (Adapter-Only) checkpoint.

Analysis of "Good" Checkpoint: Our "Good" model demonstrates successful factorization. We analyze the singular value spectrum of its conditional signal  $(y_{cond})$  (Figure 6 a), which reveals a classic "elbow" curve with an effective rank of 1. This result confirms the adapter learned an efficient, low-dimensional representation of the \*effect\*, as the base LoRA handled the domain's content. This low-rank structure is the key to generalization.

**Analysis of "Bad" Checkpoint:** In stark contrast, the adapter-only model fails. Its conditional signal  $(y_{cond})$  has a high-rank spectrum that decays slowly, mirroring the content signal  $(y_{text})$  (Figure 6 b). This is the root cause of its failure: trained in isolation, the adapter did not learn the simple effect but instead memorized the complex, high-dimensional content of the synthetic training data.

**The "Bulldozer Effect":** We term this failure mode the "Bulldozer Effect". The "Bad" adapter's signal is not only **high-rank** (content memorization) but also has a massive magnitude and is orthogonal to the backbone's content space. Instead of collaborating, the adapter represents its

memorized content in a vacant subspace. During inference, this powerful signal "bulldozes" and replaces the text signal  $(y_{\text{text}})$ , resulting in output dominated by the training scene features.

### 8. Conclusion and Future Work

As scaling laws continue to yield bigger and better pretraining of generative video models, post-training strategies will become all the more crucial in order to achieve reliable, intuitive, and controllable models for specific use cases. Our paper offers a new paradigm for thinking about the construction of useful datasets for fine-tuning video models. We show that rather than attempting to gather a dataset that is as *realistic* as possible, a better strategy may be to construct one that is as *disentangled* as possible, foregoing realism entirely. We posit that the latent representations learned by foundation models are so expressive and the priors for realism so strong, that the role of fine-tuning is coaxing out existing learned properties, interpolated somewhere in the existing latent space, rather than extrapolating and expanding the domain.

While we show the efficacy of our method on three specific control types, the general framework inspires many directions for future work. Future work could explore a unified model that learns to disentangle multiple parameters (e.g., aperture *and* temperature) from a single joint control vector. Furthermore, this data-efficient paradigm could be extended to other spatial controls, such as learning depth or pose from simple geometric data, potentially reducing the need for complex, photorealistic datasets in those domains as well.

### A. Dataset Details

**Pyramid Sampling Strategy.** We first describe our efficient sampling strategy, which balances coverage of the control space with the cost of generating synthetic scenes. Enumerating all combinations of control scalars and randomized scene settings would lead to a combinatorial explosion, so we adopt a *pyramid generation strategy* that varies the number of sampled scalars per layer while keeping the sampling distribution uniform.

Specifically, we divide the control range [-1,1] into five layers and sample 9+7+5+3+1=25 scalar values using jittered sampling, ensuring that *every point in the interval has equal probability of being selected*. For each layer, we generate six scenes using our randomized scene-generation procedure (described later in this section), and each scene is rendered across all scalar values assigned to its layer.

This results in  $6\times25=150$  total training samples. Compared to exhaustive sampling (30 scenes  $\times$  150 scalar values = 4,500 combinations), our pyramid strategy achieves a  $30\times$  reduction in data size while preserving uniform coverage of the control range and diversity across the randomized context space.

Shutter Speed. Given a sampled scalar  $c \in [-1,1]$  and a randomized scene, we synthesize videos using a simple 2D physics-based renderer. Each scene contains 1–3 colored geometric primitives (circle, square, triangle, star) moving with constant velocities on a uniform background inside a  $512 \times 512$  canvas, with elastic boundary reflections. We map c to an effective frame rate FPS(c) via a centered log mapping, and set the exposure duration to 1/FPS(c). For each output frame, we then integrate over the exposure window by temporally averaging 32 analytically predicted sub-frames, advancing the shapes according to their motion model at each sub-step. Crucially, the underlying shape trajectories and backgrounds are shared across all shutter values for a given scene, so the only changing factor along the control axis is the strength of the motion blur.

**Aperture.** For aperture control, we build a 3D depth-of-field image dataset in Blender. Each scene contains 2–4 rigid objects (cubes, spheres, cylinders, cones, pyramids) placed on a ground plane with a vertical back wall, both sharing a neutral or softly colored material. Objects are assigned distinct colors and arranged at different depths between  $d_{\min}$  and  $d_{\max}$ , forming a clear foreground-midground-background ordering. We always select one foreground object as the focus target and attach the camera's DoF focus to this object.

Given a sampled scalar  $c \in [-1, 1]$ , we map it to a physical f-number using the same centered log mapping used for shutter speed, i.e.,  $c \mapsto \mathrm{fstop}(c) \in [\mathrm{fstop_{lo}}, \mathrm{fstop_{hi}}]$ . For each scene, we then render multiple conditions by varying only the aperture  $\mathrm{fstop}(c)$  while keeping camera pose, ob-

ject geometry, materials, and lighting fixed. Lighting consists of a gray world background plus an optional point light placed on a circle around the scene (either per-scene or per-render), which introduces mild but controlled highlights without changing depth layering. This produces aligned image sets in which the foreground remains in focus while mid- and background objects exhibit depth-dependent defocus changes in accordance with the aperture control scalar.

Temperature We start from sharp 2D scenes and apply a global white-balance transformation. Each base scene consists of 2–4 colored shapes (circles, squares, triangles, stars) randomly placed on a  $512 \times 512$  canvas with a uniform background color. We first render a single reference image per scene without blur or noise. Then, for each sampled scalar  $c \in [-1,1]$ , we map c to a target color temperature  $K(c) \in [K_{lo}, K_{hi}]$  using a perceptually uniform Mired-based mapping, and apply a Kelvin-to-RGB white-balance adjustment to the entire image. The transform is defined relative to a reference neutral temperature (e.g.,  $K_{\rm ref} = 6500 \, {\rm K}$ ) and optionally re-normalized to preserve average luminance. This yields condition-aligned image sets in which geometry, layout, and background remain fixed, while only the global color cast smoothly shifts from warm to cool as a function of the temperature control scalar.

### **B.** Algorithmic Details

We provide high-level pseudocode for our model's core attention block and our data-free evaluation methodologies.

### **B.1. Jointly Trained Attention Block**

Algorithm 1 outlines the forward pass of a "WanAttention-Block" that has been adapted with our joint training strategy. It details how the base LoRA update is integrated into the backbone's weights and how the conditional signal from the "FPSCrossAttentionAdapter" is computed and combined with the text-based content signal.

### **B.2. Backbone Spectral Drift Analysis**

To support the examination of Hypothesis 1 in Section 7, we evaluate how fine-tuning modifies the backbone's attention projections. Algorithm 2 describes the "Backbone Intruder Dimension Check." This data-free method quantifies catastrophic forgetting by measuring the spectral similarity between the original pre-trained backbone weights and the final adapted backbone weights after joint training.

# **B.3. Data-Free Spectral Evaluation of the Conditional Adapter**

To complement the comparative spectral analysis of Hypothesis 2 in Section 7, we employ a data-free procedure ("Principal Component Showdown") summarized in Algorithm 3. This method constructs a diagnostic testbench directly from the model's weights by extracting the dominant

**Algorithm 1:** Forward Pass of a Jointly Trained Attention Block

```
Input: x: Input video latent features
c_{\text{text}}: Text context embedding
c_{\text{cond}}: Scalar physical condition (e.g., in [-1, 1])
W_q, W_k, W_v, W_o: Pre-trained cross-attention
weights
\Delta W_{\text{lora}}: Learned base LoRA update
Adapter<sub>cond</sub>: Trained conditional adapter module
Output: x_{\text{out}}: Updated video latent features
/\star 1. Form the final adapted
      backbone weights
W_q' \leftarrow W_q + \Delta W_{\text{lora.q}}
W_k' \leftarrow W_k + \Delta W_{\text{lora\_k}}
W_v' \leftarrow W_v + \Delta W_{\text{lora\_v}}
W_o' \leftarrow W_o + \Delta W_{\text{lora\_o}}
/* 2. Compute Query, Text Keys,
      and Text Values
q \leftarrow \text{norm}(x \cdot (W_q')^T)
K_{\text{text}} \leftarrow \text{norm}(c_{\text{text}} \cdot (W_k')^T)
V_{\text{text}} \leftarrow c_{\text{text}} \cdot (W_v')^T
/* 3. Compute the text-based
      content signal
y_{\text{text}} \leftarrow \text{Attention}(q, K_{\text{text}}, V_{\text{text}})
/* 4. Compute Conditional Keys and
      Values via Adapter
                                                                   */
e_{\text{cond}} \leftarrow \text{MLP}_{\text{cond}}(c_{\text{cond}})
K_{\text{cond}}, V_{\text{cond}} \leftarrow \text{Adapter}_{\text{cond}}(e_{\text{cond}})
/* 5. Compute the conditional
      signal
y_{\text{cond}} \leftarrow \text{Attention}(q, K_{\text{cond}}, V_{\text{cond}})
/\star 6. Combine signals with a
      learned gate g
y_{\text{combined}} \leftarrow y_{\text{text}} + g \cdot y_{\text{cond}}
/* 7. Apply final output
      projection
x_{\text{out}} \leftarrow x + y_{\text{combined}} \cdot (W_o')^T
```

principal directions of the backbone's attention projections. We then evaluate the conditional adapter's response to these canonical content directions and compute the singular value spectrum of the resulting signal.

### C. Training Details

All models are trained on NVIDIA A100 80GB (A100E) GPUs using Wan2.1-T2V-14B as the backbone with bfloat16 precision. Unless noted otherwise, we follow the same configuration across all experiments. Each run trains

Algorithm 2: Backbone Intruder Dimension Check

```
Input: W_{\text{pre}}: A pre-trained backbone weight
           matrix
W_{\rm lora}: The final adapted backbone weight matrix
(W_{\rm pre} + \Delta W_{\rm lora})
k: Number of top singular vectors to check (e.g., 64)
\epsilon: Intruder similarity threshold (e.g., 0.5)
Output: N_{\text{intruders}}: Count of detected intruder
           dimensions
/* 1. Compute SVD for both weight
     matrices
U_{\text{pre}}, \_, \_ \leftarrow \text{SVD}(W_{\text{pre}})
U_{\text{lora}}, -, - \leftarrow \text{SVD}(W_{\text{lora}})
N_{\text{intruders}} \leftarrow 0
/\star 2. Check top-k vectors of the
     adapted backbone
for j \leftarrow 1 to k do
     u_{\text{lora}_{-j}} \leftarrow j-th column of U_{\text{lora}}
     /* 3. Find max similarity to
          any pre-trained vector
     S_{\text{max}} \leftarrow 0
    for i \leftarrow 1 to number of columns in U_{pre} do
         u_{\text{pre}_{-i}} \leftarrow i\text{-th column of }U_{\text{pre}}
         s \leftarrow abs(cosine\_similarity(u_{lora\_j}, u_{pre\_i}))
         S_{\max} \leftarrow \max(S_{\max}, s)
     /* 4. Count as intruder if
          similarity is below threshold
          */
    if S_{max} < \epsilon then
         N_{\text{intruders}} \leftarrow N_{\text{intruders}} + 1
return N_{intruders}
```

for up to 1000 epochs with a micro-batch size of 1 per GPU, gradient accumulation of 4, and a single pipeline stage. This corresponds to a global batch size of 4 and yields roughly 18,000 training steps for our 30 shots synthetic datasets. Under this setup, each pyramid training stage completes in approximately one day on two A100E.

We use four condition-adapter tokens, an adapter embedding dimension of 256, and LoRA rank 32 for both the condition adapters and the backbone LoRA, with the adapter gate fixed at 0.5 throughout training. A learning rate of  $2\times10^{-5}$  with a 100-step warmup is applied. Optimization is performed using the AdamW optimizer[20] with betas (0.9,0.99), weight decay 0.01, and  $\varepsilon=10^{-8}$ . All LoRA and adapter parameters are trained in bfloat16 with activation checkpointing enabled for memory efficiency.

# **Algorithm 3:** Data-Free Spectral Rank Analysis ("*Principal Component Showdown*")

**Input**:  $W'_q, W'_k, W'_v$ : final adapted backbone

Adapter<sub>cond</sub>: trained conditional adapter module  $c_{\text{strong}}$ : a strong condition value (e.g., c = 1.0)

projection weights

```
N: number of principal components to test (e.g.,
N = 64
Output: S_{\text{text}}, S_{\text{cond}}: normalized singular value
\mathcal{R}_{text}, \mathcal{R}_{cond}: effective ranks of backbone and
conditional signals
/* 1.
             Extract principal content
      primitives from the backbone
U_q, \_, \_ \leftarrow \text{SVD}((W_q')^T)
U_k, -, - \leftarrow \text{SVD}((W_k')^T)
U_v, \_, \_ \leftarrow \text{SVD}((W_v')^T)
q_{\text{test}} \leftarrow \text{TopN}(U_q, N)
k_{\text{text\_test}} \leftarrow \text{TopN}(U_k, N)
v_{\text{text\_test}} \leftarrow \text{TopN}(U_v, N)
/* 2. Simulate backbone response
      to principal content directions
y_{\text{text\_principal}} \leftarrow \text{Attention}(q_{\text{test}}, k_{\text{text\_test}}, v_{\text{text\_test}})
/* 3. Generate and simulate
      conditional response
K_{\text{cond}}, V_{\text{cond}} \leftarrow \text{Adapter}_{\text{cond}}(c_{\text{strong}})
y_{\text{cond-principal}} \leftarrow \text{Attention}(q_{\text{test}}, K_{\text{cond}}, V_{\text{cond}})
```

```
Normalize S_{\text{text}}, S_{\text{cond}} by their leading singular values 

/* 5. Estimate effective ranks */
\mathcal{R}_{\text{text}} \leftarrow \text{EffectiveRank}(S_{\text{text}})
\mathcal{R}_{\text{cond}} \leftarrow \text{EffectiveRank}(S_{\text{cond}})
return S_{\text{text}}, S_{\text{cond}}, \mathcal{R}_{\text{text}}, \mathcal{R}_{\text{cond}}
```

/\* 4. Compute singular value

 $S_{\text{text}}, \leftarrow \text{SVD}(\text{flatten}(y_{\text{text\_principal}}))$ 

 $S_{\text{cond}}, \leftarrow \text{SVD}(\text{flatten}(y_{\text{cond\_principal}}))$ 

### **D.** Experiment Details

spectra

In this section, we provide additional details for the experimental comparisons introduced in Section 6.

### D.1. Group 1: Data Complexity (Syn. vs. Real)

**Dataset Construction.** For the Group 1 comparison, we adopt a controlled one-shot setting in which each physical effect (shutter speed, aperture, temperature) is represented by a single scene containing seven scalar conditions that

# A horse and rider jumping over an obstacle during an equestrian event, captured in bright daylight with a clear blue sky. A perture A young woman in a fazzy brown jacket and winter hat holds a cup at a lively outdoor Christmas market. Synthetic Dataset Shutter A perture Temperature A vibrant field of purple lupine flowers leads the eye to the rugged, majestic Vestrahorn mountains in Iceland, all under a dynamic sky with dramatic clouds. Synthetic Dataset Temperature Temperature Temperature

Figure 7. Comparison of the photorealistic and synthetic one-shot datasets used in Group 1. For each physical effect (shutter speed, aperture, temperature), we show the two extreme control values (c=-1 and c=1). Although only the endpoints are visualized, each dataset contains seven aligned conditions in total within the normalized range  $c \in [-1, 1]$ .

are aligned across the synthetic and photorealistic datasets (see Figure 7). All conditions are normalized to the shared range  $c \in [-1,1]$ , ensuring that both datasets express identical control values despite differences in rendering styles.

**Evaluation Prompt Details.** Following the prompt construction strategy used in VBench—which we also rely on for the FEP metric—we generate a diverse set of 96 motion-centric T2V prompts using an LLM (Gemini 2.5). The prompts span eight categories (animals, architecture, food, humans, lifestyle, plants, scenery, and vehicles), with 12 prompts per category. We use this set to evaluate SVP under a broad range of motion patterns and scene types.

Quantitative Results Recap. As shown in Figure 4, models fine-tuned on our simple synthetic dataset exhibit substantially smaller drift from the pretrained backbone when monitored using the FEP metrics (Section 5.1). In contrast, training on the photorealistic dataset leads to noticeably larger and faster deviation throughout training. This difference in drift is reflected in the final SVP results (Section 5.2): the model trained on synthetic data maintains near-baseline semantic fidelity, while the model trained on photorealistic data shows clear backbone degradation. These findings highlight that, for learning physical controls, low-complexity synthetic data provides a more stable and robust supervision signal.

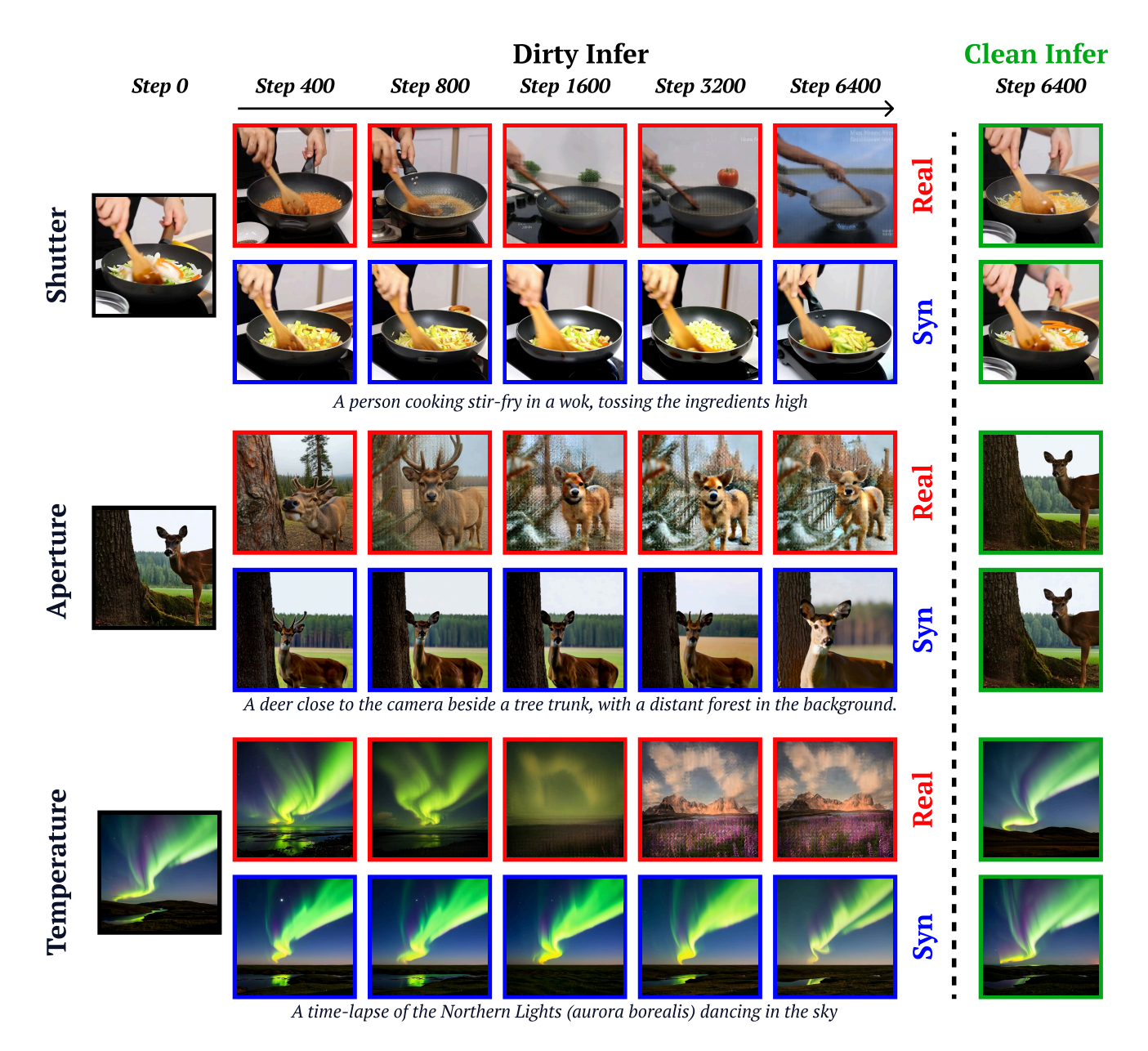


Figure 8. Visual comparison of backbone corruption during training. The synthetic-trained model remains stable and continues to follow the input prompt, whereas the model trained on photorealistic data rapidly drifts toward copying its training scene (see Fig. 7). This manifests as semantic drift, texture collapse, and global color shifts that intensify over training.

Visualization Evaluation. Beyond the quantitative trends, the backbone degradation becomes most apparent when inspecting the model's inference outputs during training (see Figure 8). When trained on our synthetic dataset, the model continues to follow the input prompt and preserves the overall appearance of the generated scene. In contrast, the model trained on the photorealistic dataset begins to visually drift toward the training images themselves: details, textures, and global color tones increasingly resemble the underlying photorealistic scene rather than the prompted

content. This "copying" behavior appears early in training and progressively intensifies, manifesting as semantic drift, texture collapse, and color hallucination. These visual failures provide an intuitive counterpart to the backbone corruption measured by our FEP and SVP metrics.

# D.2. Group 2: Inference Strategy (Decoupled vs. Joint)

While Group 1 highlights the stability advantage of synthetic data during training, here we analyze how inference

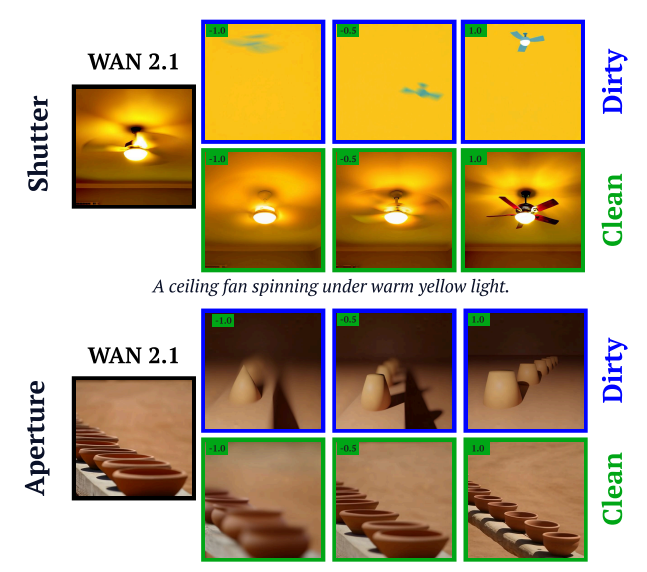
strategy further affects the final output quality. Specifically, we compare the joint inference procedure ("dirty inference"), which directly passes the adapter-modulated activations into the backbone, against our proposed decoupled inference method ("clean inference") method, which prunes the shallow DiT blocks, removing the residual content drift before decoding.

Quantitative Results Recap. Similar to the quantitative trends observed in Group 1, the metrics in Group 2 also reveal a clear advantage for our clean inference strategy. As summarized in Table 1 and the corresponding FEP/SVP curves and charts in Figure 4, clean inference consistently yields lower drift and higher semantic fidelity compared to dirty inference across all physical controls. Even when the model is trained on the synthetic dataset—where backbone corruption is already minimal—clean inference further reduces the residual deviations and restores the model's output closer to the original WAN 2.1 behavior. These quantitative results motivate a closer look at the visual differences between the two inference modes.

Visual Evidence. The visual comparisons further reinforce the quantitative trends. As shown in the last column of Figure 8, applying clean inference to a corrupted checkpoint trained on photorealistic data dramatically restores prompt fidelity and global appearance: the model no longer copies textures or colors from the training scene, and semantic drift is substantially reduced. This demonstrates that much of the degradation observed during training is not permanently baked into the weights but instead arises from residual content leakage that clean inference effectively removes.

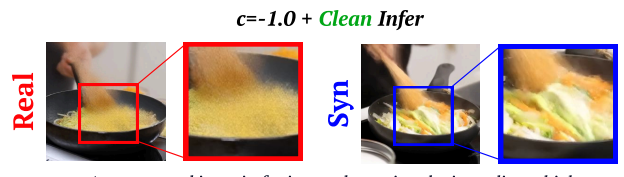
A similar pattern appears even when the model is trained on the synthetic dataset. Although backbone corruption is minimal in this setting, and the model is capable of yielding high-quality output as shown in Figure 3, dirty inference still injects subtle synthetic-style bias—such as flattened textures or blurred shading—into the final output. As shown in Figure 9, clean inference suppresses these artifacts and produces videos that closely match the visual style and sharpness of the original WAN 2.1 backbone across different control values.

Limitations of Real Data. Although clean inference substantially reduces the corruption introduced by real-data training, it does not fully eliminate it—especially under extreme control values. As shown in Figure 10, the model trained on the real shutter speed dataset still exhibits noise and structural artifacts when the control approaches the boundaries (e.g., c=-1.0), even after applying clean inference. This occurs because the real sequence contains complex high-entropy motion: articulated limbs, nonlinear trajectories, and strong background parallax. In contrast, the synthetic shutter speed dataset is constructed from simple rigid motion with clean parametric trajectories, providing a



A line of clay plots arranged from near to far on a stong ledge, the camera focusing on one clay pot.

Figure 9. Effect of clean vs. dirty inference on a model trained with the synthetic pyramid dataset. Although synthetic training induces only mild backbone drift, dirty inference still injects subtle synthetic-style biases (e.g., flattened shading and softened textures) into the outputs. Applying clean inference removes these artifacts and restores the visual style of the original WAN 2.1 model across different control values.

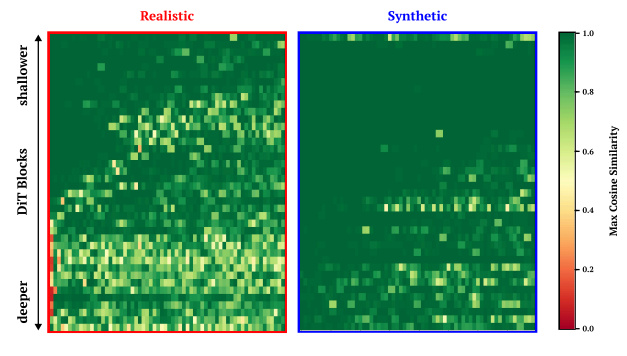


A person cooking stir-fry in a wok, tossing the ingredients high

Figure 10. Visual comparison of backbone corruption during training. The synthetic-trained model remains stable and continues to follow the input prompt, whereas the model trained on photorealistic data rapidly drifts toward copying its training scene (see Fig. 7). This manifests as semantic drift, texture collapse, and global color shifts that intensify over training.

much more disentangled supervision signal.

These observations reinforce our *Less is More* thesis: low-complexity synthetic data is inherently easier for the model to factorize and scales reliably across the full control range, whereas real data introduces irreducible entanglement that clean inference can mitigate but not fully correct. Thus, synthetic data remains the preferred choice for learning stable, well-behaved physical controls.



(a) Similarity Heatmap Comparison

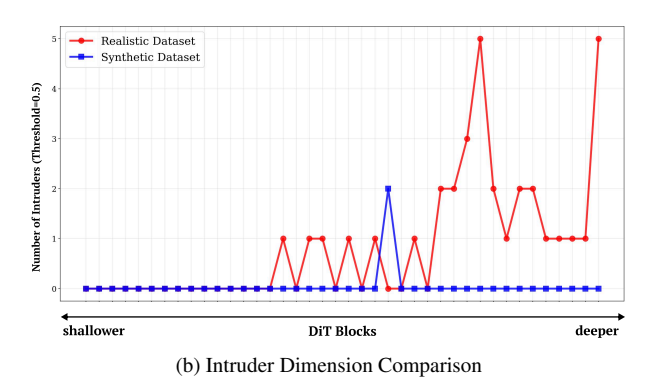


Figure 11. Backbone content drift across depth for the shutter speed condition. Analysis performed on the value projection  $W_v$ . (a) Max cosine similarity between content directions and FPS-conditioned features. (b) Number of content intruders (cosine > 0.5).

### E. Analysis Details

# E.1. Hypothesis 1: The Spectrum of Backbone Adaptation

Expanding on Hypothesis 1 in Section 7, we analyze how the complexity of fine-tuning data influences the backbone's spectral drift under conditional adaptation. Unless otherwise noted, all measurements are performed on the value projection  $W_v$ , though we observe qualitatively similar trends in  $W_q$ ,  $W_k$ , and  $W_o$ . Figure 11 reports the results for the shutter speed condition using both real and synthetic training data as discussed in Sec. D. Other physical controls exhibit the same overall behavior: simple synthetic data preserves the pretrained spectral structure, whereas complex real data drives substantial high-rank intrusions into the backbone.

Clean Adaptation (Single Synthetic Scene). As shown in Fig. 11a, synthetic shutter speed conditioning results in minimal drift throughout the network. The similarity heatmap remains uniformly low (green), indicating that the

adapter modifies  $W_v$  through small non-destructive adjustments. This corresponds to a clean and stable form of adaptation: the model adjusts to the new condition while largely preserving the pretrained spectral structure. However, the specialization remains narrow, as the synthetic data contains only one simple scene.

Catastrophic Forgetting (Single Complex Scene). In contrast, Fig. 11b reveals that real shutter conditioning induces substantial spectral drift in  $W_v$ , particularly in shallow and mid-depth blocks. A large number of high-similarity intruders (cosine similarity > 0.5) appear as early as blocks 0–12 and accumulate into dense clusters in deeper layers. This is the hallmark of catastrophic forgetting: the model learns strong, scene-specific features that overwrite general-purpose representations. These intruder directions propagate into the conditioned path during inference, producing the "ghosting" artifacts seen in the qualitative comparisons. Similar behavior appears under other real-data conditions.

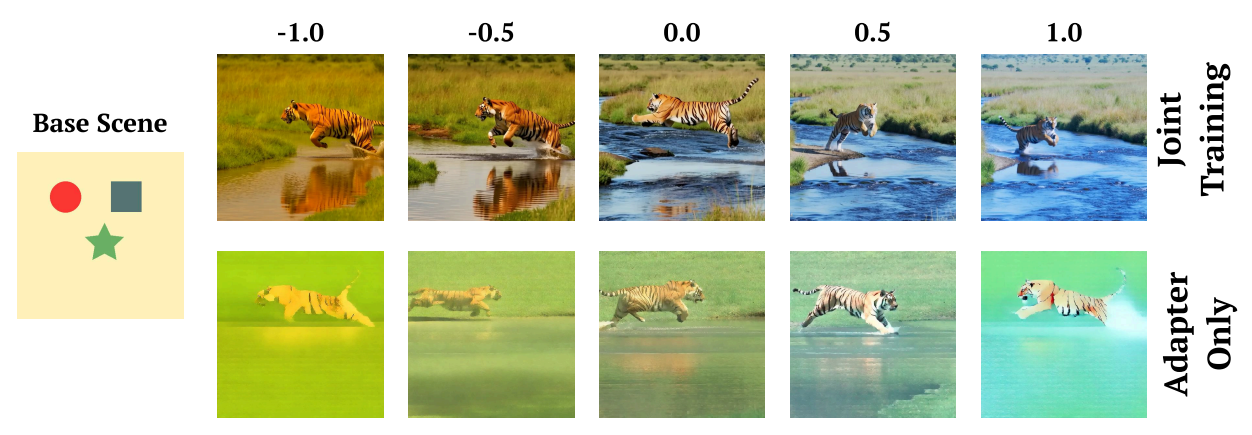
Overall, this data-free analysis corroborates our quantitative findings and highlights that deeper blocks inherently provide cleaner, more stable channels for condition modulation.

# **E.2. Hypothesis 2: Adapter-Only Training Entangles Context and Condition**

In Hypothesis 2 from Section 7, our comparative spectral analysis showed that the "Good" (jointly trained) checkpoint produces a low-rank, effect-specific conditional signal, whereas the "Bad" (adapter-only) checkpoint produces a high-rank signal that mixes effect and training-scene content. To visualize how this structural difference affects behavior, we evaluate both models on the same one-shot temperature-conditioned synthetic dataset used during training.

Although the dataset is extremely small (1 scene and 7 conditions), both models still learn the temperature effect to a noticeable degree. The purpose of this experiment is not to evaluate the realism of temperature control, but to examine whether each training strategy can express the effect cleanly, without unintentionally altering unrelated scene content.

Adapter-Only Training (High-Rank Conditional Signal). As shown in Fig. 12, varying the temperature condition  $c \in [-1,1]$  causes the adapter-only model to drift away from the original scene: color tone changes are partially entangled with shifts in background structure and global appearance. While the temperature effect itself is present, it is accompanied by unintended modifications to the scene. This matches our spectral findings: the high-rank conditional signal encodes both the intended effect and the



A tiger jumps over a water stream.

Figure 12. **Hypothesis 2:** Adapter-only training entangles condition and context. On the one-shot temperature-conditioned synthetic dataset, both models learn some temperature effect, but the adapter-only model introduces unintended scene drift, whereas joint training yields clean, isolated temperature changes.

training-scene context, which becomes increasingly dominant as  $\left|c\right|$  increases.

**Joint Backbone and Adapter Training (Low-Rank Conditional Signal).** In contrast, the jointly trained model expresses the same learned temperature effect more cleanly. As c varies, the scene content remains stable, and most changes are confined to the desired color-temperature direction. Despite the one-shot nature of the dataset, the jointly trained model avoids leaking training-scene content into the conditional pathway. This aligns with the low-rank spectrum observed in Figure 6, where the effect is captured in a compact direction that interacts with the backbone without re-encoding context.

Overall, even with limited one-shot synthetic data, this diagnostic highlights a consistent pattern: joint training preserves context and isolates the intended effect, whereas adapter-only training entangles the two.

### F. Example Gallery

Figure 13 presents a diverse set of examples generated with our shutter-, aperture-, and temperature-controlled T2V framework. Each physical control is parameterized within a unified range  $c \in [-1,1]$ , enabling smooth and interpretable adjustments to motion blur, depth of field, and color tone. Across a wide variety of scenes and prompts, the outputs change in a consistent and approximately monotonic manner as c varies, demonstrating the reliability and generality of our learned control space.

To further assess this generalization, Figures 14, 15 and 17 evaluate each control dimension in more challenging scenarios. Shutter control extends to moving-camera settings and scenes with multiple independently moving ob-

jects, while maintaining predictable blur variation. Aperture control remains stable across diverse depth layouts and can shift focus to locations beyond the foreground, producing smooth boken shifts as depth varies (see Figure 16). Temperature control remains consistent across indoor environments and highly stylized domains such as anime and pixel art. Together, these results show that our learned controls generalize far beyond the simple one-shot synthetic scenes used for training.

### References

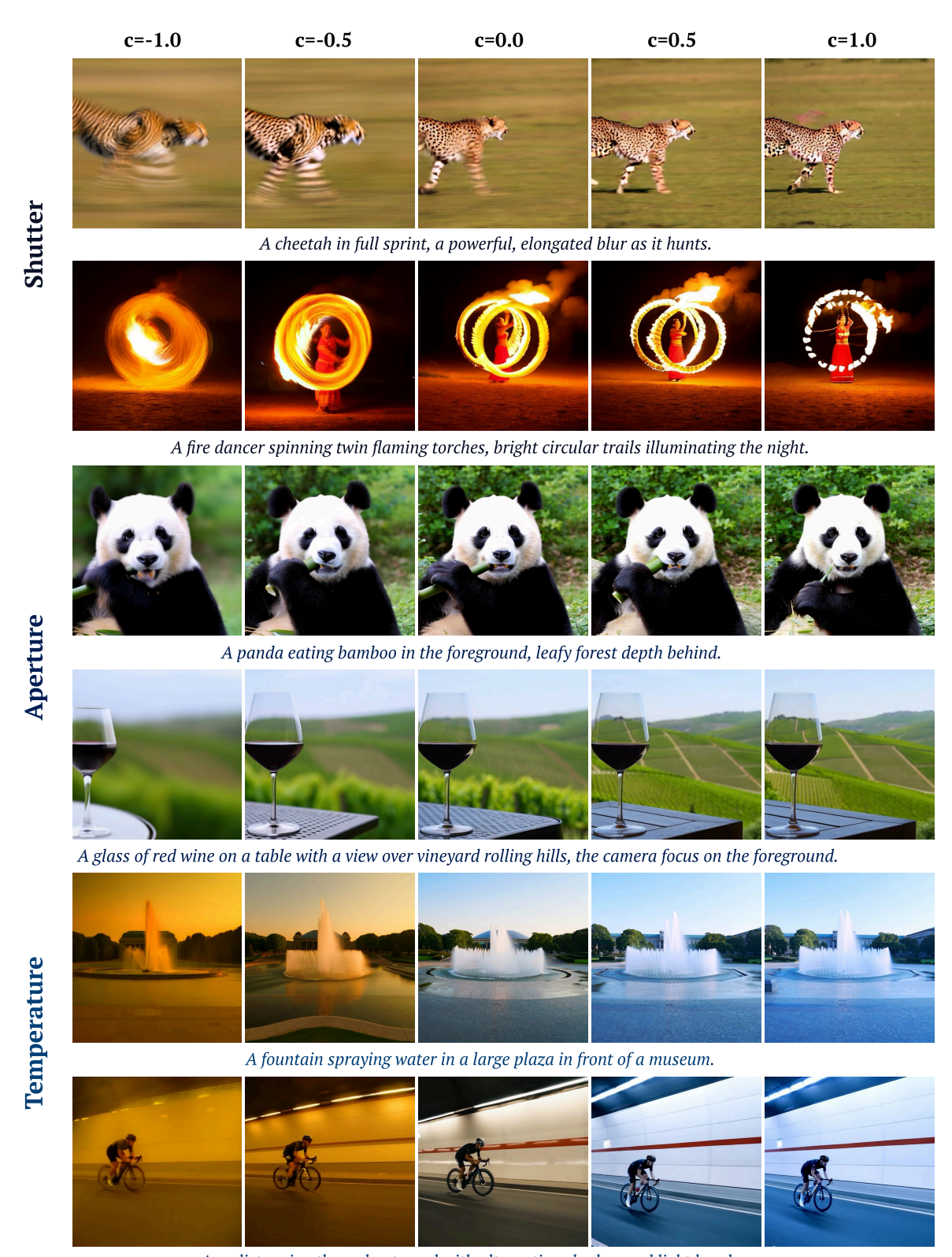
- [1] Jianhong Bai, Menghan Xia, Xiao Fu, Xintao Wang, Lianrui Mu, Jinwen Cao, Zuozhu Liu, Haoji Hu, Xiang Bai, Pengfei Wan, et al. Recammaster: Camera-controlled generative rendering from a single video. *arXiv preprint arXiv:2503.11647*, 2025. 1
- [2] Shariq Farooq Bhat, Niloy Mitra, and Peter Wonka. Loosecontrol: Lifting controlnet for generalized depth conditioning. In ACM SIGGRAPH 2024 Conference Papers, pages 1–11, 2024. 2
- [3] Gang Cheng, Xin Gao, Li Hu, Siqi Hu, Mingyang Huang, Chaonan Ji, Ju Li, Dechao Meng, Jinwei Qi, Penchong Qiao, et al. Wan-animate: Unified character animation and replacement with holistic replication. arXiv preprint arXiv:2509.14055, 2025. 1
- [4] Guillaume Couairon, Jakob Verbeek, Holger Schwenk, and Matthieu Cord. Diffedit: Diffusion-based semantic image editing with mask guidance. *arXiv preprint arXiv:2210.11427*, 2022. 2
- [5] Alexey Dosovitskiy, Philipp Fischer, Eddy Ilg, Philip Hausser, Caner Hazirbas, Vladimir Golkov, Patrick Van Der Smagt, Daniel Cremers, and Thomas Brox. Flownet: Learning optical flow with convolutional networks. In *Proceedings of the IEEE international conference on computer vision*, pages 2758–2766, 2015.

- [6] I-Sheng Fang, Yue-Hua Han, and Jun-Cheng Chen. Camera settings as tokens: Modeling photography on latent diffusion models. In SIGGRAPH Asia 2024 Conference Papers, 2024.
- [7] Armando Fortes, Tianyi Wei, Shangchen Zhou, and Xingang Pan. Bokeh diffusion: Defocus blur control in text-to-image diffusion models. *arXiv preprint arXiv:2503.08434*, 2025. 2, 6, 7
- [8] Michal Geyer, Omer Bar-Tal, Shai Bagon, and Tali Dekel. Tokenflow: Consistent diffusion features for consistent video editing. arXiv preprint arXiv:2307.10373, 2023. 2
- [9] Xi Guo, Wei Wu, Dongliang Wang, Jing Su, Haisheng Su, Weihao Gan, Jian Huang, and Qin Yang. Learning video representations of human motion from synthetic data. In Proceedings of the IEEE/CVF Conference on Computer Vision and Pattern Recognition, pages 20197–20207, 2022. 2
- [10] Yuwei Guo, Ceyuan Yang, Anyi Rao, Zhengyang Liang, Yaohui Wang, Yu Qiao, Maneesh Agrawala, Dahua Lin, and Bo Dai. Animatediff: Animate your personalized textto-image diffusion models without specific tuning. arXiv preprint arXiv:2307.04725, 2023. 2
- [11] Hao He, Yinghao Xu, Yuwei Guo, Gordon Wetzstein, Bo Dai, Hongsheng Li, and Ceyuan Yang. Cameractrl: Enabling camera control for text-to-video generation. *arXiv preprint arXiv:2404.02101*, 2024. 2
- [12] Jonathan Ho, Ajay Jain, and Pieter Abbeel. Denoising diffusion probabilistic models. Advances in neural information processing systems, 33:6840–6851, 2020. 2
- [13] Edward J Hu, Yelong Shen, Phillip Wallis, Zeyuan Allen-Zhu, Yuanzhi Li, Shean Wang, Lu Wang, Weizhu Chen, et al. Lora: Low-rank adaptation of large language models. *ICLR*, 1(2):3, 2022.
- [14] Ziqi Huang, Yinan He, Jiashuo Yu, Fan Zhang, Chenyang Si, Yuming Jiang, Yuanhan Zhang, Tianxing Wu, Qingyang Jin, Nattapol Chanpaisit, et al. Vbench: Comprehensive benchmark suite for video generative models. In *Proceedings of* the IEEE/CVF Conference on Computer Vision and Pattern Recognition, pages 21807–21818, 2024. 2
- [15] Zeyinzi Jiang, Zhen Han, Chaojie Mao, Jingfeng Zhang, Yulin Pan, and Yu Liu. Vace: All-in-one video creation and editing. *arXiv preprint arXiv:2503.07598*, 2025. 1
- [16] Yo-whan Kim, Samarth Mishra, SouYoung Jin, Rameswar Panda, Hilde Kuehne, Leonid Karlinsky, Venkatesh Saligrama, Kate Saenko, Aude Oliva, and Rogerio Feris. How transferable are video representations based on synthetic data? Advances in Neural Information Processing Systems, 35:35710–35723, 2022. 2
- [17] Weijie Kong, Qi Tian, Zijian Zhang, Rox Min, Zuozhuo Dai, Jin Zhou, Jiangfeng Xiong, Xin Li, Bo Wu, Jianwei Zhang, et al. Hunyuanvideo: A systematic framework for large video generative models. *arXiv preprint arXiv:2412.03603*, 2024.
- [18] Yuheng Li, Haotian Liu, Qingyang Wu, Fangzhou Mu, Jianwei Yang, Jianfeng Gao, Chunyuan Li, and Yong Jae Lee. Gligen: Open-set grounded text-to-image generation. In Proceedings of the IEEE/CVF conference on computer vision and pattern recognition, pages 22511–22521, 2023. 2

- [19] Zhiqiu Lin, Deepak Pathak, Baiqi Li, Jiayao Li, Xide Xia, Graham Neubig, Pengchuan Zhang, and Deva Ramanan. Evaluating text-to-visual generation with image-to-text generation. In *European Conference on Computer Vision*, pages 366–384. Springer, 2024. 2, 4
- [20] Ilya Loshchilov and Frank Hutter. Decoupled weight decay regularization. arXiv preprint arXiv:1711.05101, 2017. 2
- [21] Nikolaus Mayer, Eddy Ilg, Philipp Fischer, Caner Hazirbas, Daniel Cremers, Alexey Dosovitskiy, and Thomas Brox. What makes good synthetic training data for learning disparity and optical flow estimation? *International Journal of Computer Vision*, 126(9):942–960, 2018.
- [22] Chong Mou, Xintao Wang, Liangbin Xie, Yanze Wu, Jian Zhang, Zhongang Qi, and Ying Shan. T2i-adapter: Learning adapters to dig out more controllable ability for text-to-image diffusion models. In *Proceedings of the AAAI conference on artificial intelligence*, pages 4296–4304, 2024. 2
- [23] Bolin Ni, Houwen Peng, Minghao Chen, Songyang Zhang, Gaofeng Meng, Jianlong Fu, Shiming Xiang, and Haibin Ling. Expanding language-image pretrained models for general video recognition. In *European conference on computer vision*, pages 1–18. Springer, 2022. 2, 4
- [24] OpenAI. Video generation models as world simulators. https://openai.com/index/videogeneration-models-as-world-simulators/, 2024. 2
- [25] Dongwon Park, Hayeon Kim, and Se Young Chun. Contribution-based low-rank adaptation with pre-training model for real image restoration. In *European Conference* on Computer Vision, pages 87–105. Springer, 2024. 2
- [26] William Peebles and Saining Xie. Scalable diffusion models with transformers. In Proceedings of the IEEE/CVF international conference on computer vision, pages 4195–4205, 2023. 2
- [27] Juewen Peng, Zhiguo Cao, Xianrui Luo, Hao Lu, Ke Xian, and Jianming Zhang. Bokehme: When neural rendering meets classical rendering. In *Proceedings of the IEEE/CVF International Conference on Computer Vision and Pattern Recognition (CVPR)*, 2022. 3
- [28] Adam Polyak, Amit Zohar, Andrew Brown, Andros Tjandra, Animesh Sinha, Ann Lee, Apoorv Vyas, Bowen Shi, Chih-Yao Ma, Ching-Yao Chuang, et al. Movie gen: A cast of media foundation models. arXiv preprint arXiv:2410.13720, 2024. 1
- [29] Chenyang Qi, Xiaodong Cun, Yong Zhang, Chenyang Lei, Xintao Wang, Ying Shan, and Qifeng Chen. Fatezero: Fusing attentions for zero-shot text-based video editing. In Proceedings of the IEEE/CVF International Conference on Computer Vision, pages 15932–15942, 2023. 2
- [30] Alec Radford, Jong Wook Kim, Chris Hallacy, Aditya Ramesh, Gabriel Goh, Sandhini Agarwal, Girish Sastry, Amanda Askell, Pamela Mishkin, Jack Clark, et al. Learning transferable visual models from natural language supervision. In *International conference on machine learning*, pages 8748–8763. PmLR, 2021. 2
- [31] Yixuan Ren, Yang Zhou, Jimei Yang, Jing Shi, Difan Liu, Feng Liu, Mingi Kwon, and Abhinav Shrivastava.

- Customize-a-video: One-shot motion customization of text-to-video diffusion models. In *European Conference on Computer Vision*, pages 332–349. Springer, 2024. 2
- [32] Olaf Ronneberger, Philipp Fischer, and Thomas Brox. Unet: Convolutional networks for biomedical image segmentation. In *International Conference on Medical image computing and computer-assisted intervention*, pages 234–241. Springer, 2015. 2
- [33] Runway. Gen-3. https://runwayml.com/, 2024. 2
- [34] Reece Shuttleworth, Jacob Andreas, Antonio Torralba, and Pratyusha Sharma. Lora vs full fine-tuning: An illusion of equivalence. arXiv preprint arXiv:2410.21228, 2024. 6
- [35] Reece Shuttleworth, Jacob Andreas, Antonio Torralba, and Pratyusha Sharma. LoRA vs full fine-tuning: An illusion of equivalence, 2025. 2
- [36] Jascha Sohl-Dickstein, Eric Weiss, Niru Maheswaranathan, and Surya Ganguli. Deep unsupervised learning using nonequilibrium thermodynamics. In *International conference on machine learning*, pages 2256–2265. pmlr, 2015. 2
- [37] Lingchen Sun, Rongyuan Wu, Zhiyuan Ma, Shuaizheng Liu, Qiaosi Yi, and Lei Zhang. Pixel-level and semantic-level adjustable super-resolution: A dual-lora approach. In *Proceed*ings of the Computer Vision and Pattern Recognition Conference, pages 2333–2343, 2025. 2
- [38] Kuaishou Technology. Kling ai. https://klingai. kuaishou.com/, 2024. 2
- [39] Yonglong Tian, Lijie Fan, Kaifeng Chen, Dina Katabi, Dilip Krishnan, and Phillip Isola. Learning vision from models rivals learning vision from data. In *Proceedings of the IEEE/CVF conference on computer vision and pattern recognition*, pages 15887–15898, 2024. 2
- [40] Thomas Unterthiner, Sjoerd Van Steenkiste, Karol Kurach, Raphael Marinier, Marcin Michalski, and Sylvain Gelly. Towards accurate generative models of video: A new metric & challenges. arXiv preprint arXiv:1812.01717, 2018. 2
- [41] Thomas Unterthiner, Sjoerd Van Steenkiste, Karol Kurach, Raphaël Marinier, Marcin Michalski, and Sylvain Gelly. Fvd: A new metric for video generation. 2019. 2
- [42] Andrey Voynov, Kfir Aberman, and Daniel Cohen-Or. Sketch-guided text-to-image diffusion models. In *ACM SIG-GRAPH 2023 conference proceedings*, pages 1–11, 2023. 2
- [43] Team Wan, Ang Wang, Baole Ai, Bin Wen, Chaojie Mao, Chen-Wei Xie, Di Chen, Feiwu Yu, Haiming Zhao, Jianxiao Yang, et al. Wan: Open and advanced large-scale video generative models. *arXiv preprint arXiv:2503.20314*, 2025. 1, 2, 5, 6
- [44] Su Wang, Chitwan Saharia, Ceslee Montgomery, Jordi Pont-Tuset, Shai Noy, Stefano Pellegrini, Yasumasa Onoe, Sarah Laszlo, David J Fleet, Radu Soricut, et al. Imagen editor and editbench: Advancing and evaluating text-guided image inpainting. In Proceedings of the IEEE/CVF conference on computer vision and pattern recognition, pages 18359– 18369, 2023. 2
- [45] Zhouxia Wang, Ziyang Yuan, Xintao Wang, Yaowei Li, Tianshui Chen, Menghan Xia, Ping Luo, and Ying Shan. Motionctrl: A unified and flexible motion controller for video generation. In ACM SIGGRAPH 2024 Conference Papers, pages 1–11, 2024. 2

- [46] Jay Zhangjie Wu, Yixiao Ge, Xintao Wang, Stan Weixian Lei, Yuchao Gu, Yufei Shi, Wynne Hsu, Ying Shan, Xiaohu Qie, and Mike Zheng Shou. Tune-a-video: One-shot tuning of image diffusion models for text-to-video generation. In Proceedings of the IEEE/CVF international conference on computer vision, pages 7623–7633, 2023. 2
- [47] Ruiqi Wu, Liangyu Chen, Tong Yang, Chunle Guo, Chongyi Li, and Xiangyu Zhang. Lamp: Learn a motion pattern for few-shot video generation. In *Proceedings of the IEEE/CVF* conference on computer vision and pattern recognition, pages 7089–7098, 2024. 2
- [48] Honghui Yang, Di Huang, Wei Yin, Chunhua Shen, Haifeng Liu, Xiaofei He, Binbin Lin, Wanli Ouyang, and Tong He. Depth any video with scalable synthetic data. *arXiv preprint arXiv:2410.10815*, 2024. 2
- [49] Shuai Yang, Yifan Zhou, Ziwei Liu, and Chen Change Loy. Rerender a video: Zero-shot text-guided video-to-video translation. In *SIGGRAPH Asia 2023 Conference Papers*, pages 1–11, 2023. 2
- [50] Hu Ye, Jun Zhang, Sibo Liu, Xiao Han, and Wei Yang. Ip-adapter: Text compatible image prompt adapter for text-to-image diffusion models. arXiv preprint arXiv:2308.06721, 2023. 3
- [51] Wangbo Yu, Jinbo Xing, Li Yuan, Wenbo Hu, Xiaoyu Li, Zhipeng Huang, Xiangjun Gao, Tien-Tsin Wong, Ying Shan, and Yonghong Tian. Viewcrafter: Taming video diffusion models for high-fidelity novel view synthesis. arXiv preprint arXiv:2409.02048, 2024. 2
- [52] Xueyang Yu, Xinlei Chen, and Yossi Gandelsman. Learning video representations without natural videos. arXiv preprint arXiv:2410.24213, 2024. 2
- [53] Yu Yuan, Xijun Wang, Yichen Sheng, Prateek Chennuri, Xingguang Zhang, and Stanley Chan. Generative photography: Scene-consistent camera control for realistic text-toimage synthesis. arXiv preprint arXiv: 2412.02168, 2024. 2, 6, 7
- [54] Fan Zhang, Shulin Tian, Ziqi Huang, Yu Qiao, and Ziwei Liu. Evaluation agent: Efficient and promptable evaluation framework for visual generative models. arXiv preprint arXiv:2412.09645, 2024. 5
- [55] Lvmin Zhang, Anyi Rao, and Maneesh Agrawala. Adding conditional control to text-to-image diffusion models. In Proceedings of the IEEE/CVF international conference on computer vision, pages 3836–3847, 2023. 2
- [56] Yisu Zhang, Chenjie Cao, Chaohui Yu, and Jianke Zhu. LiON-LoRA: Rethinking LoRA fusion to unify controllable spatial and temporal generation for video diffusion. In Proceedings of the IEEE/CVF International Conference on Computer Vision, pages 14569–14579, 2025. 2
- [57] Yang Zheng, Adam W Harley, Bokui Shen, Gordon Wetzstein, and Leonidas J Guibas. Pointodyssey: A large-scale synthetic dataset for long-term point tracking. In Proceedings of the IEEE/CVF International Conference on Computer Vision, pages 19855–19865, 2023. 2



A cyclist racing through a tunnel with alternating shadow and light bands.

Figure 13. Qualitative results of our controllable generation. Our model demonstrates precise and continuous control over shutter speed (Row 1-2, motion blur), aperture (Row 3-4, bokeh), and color temperature (Row 5-6) by varying the conditional input c from -1.0 to 1.0 across diverse, high-fidelity video prompts.

### Camera Follow & First Person View A sports car drifting around a corner, the camera following the A first-person drone view flying quickly through a large stone arch front bumper as the road moves quickly around the curve. bridge. **Shutter Shutter** longer shorter longer shorter **Multiple Objects** A flock of thousands of birds suddenly taking flight from a single A time-lapse of crowds of people rushing through an open-air tree, exploding outwards in all directions. market, examining stalls.

Figure 14. **Generalization of shutter control to scenes with complex motion.** The model responds reliably to the shutter scalar in settings involving moving cameras (e.g., camera-follow and first-person views) and scenes with multiple independently moving objects.

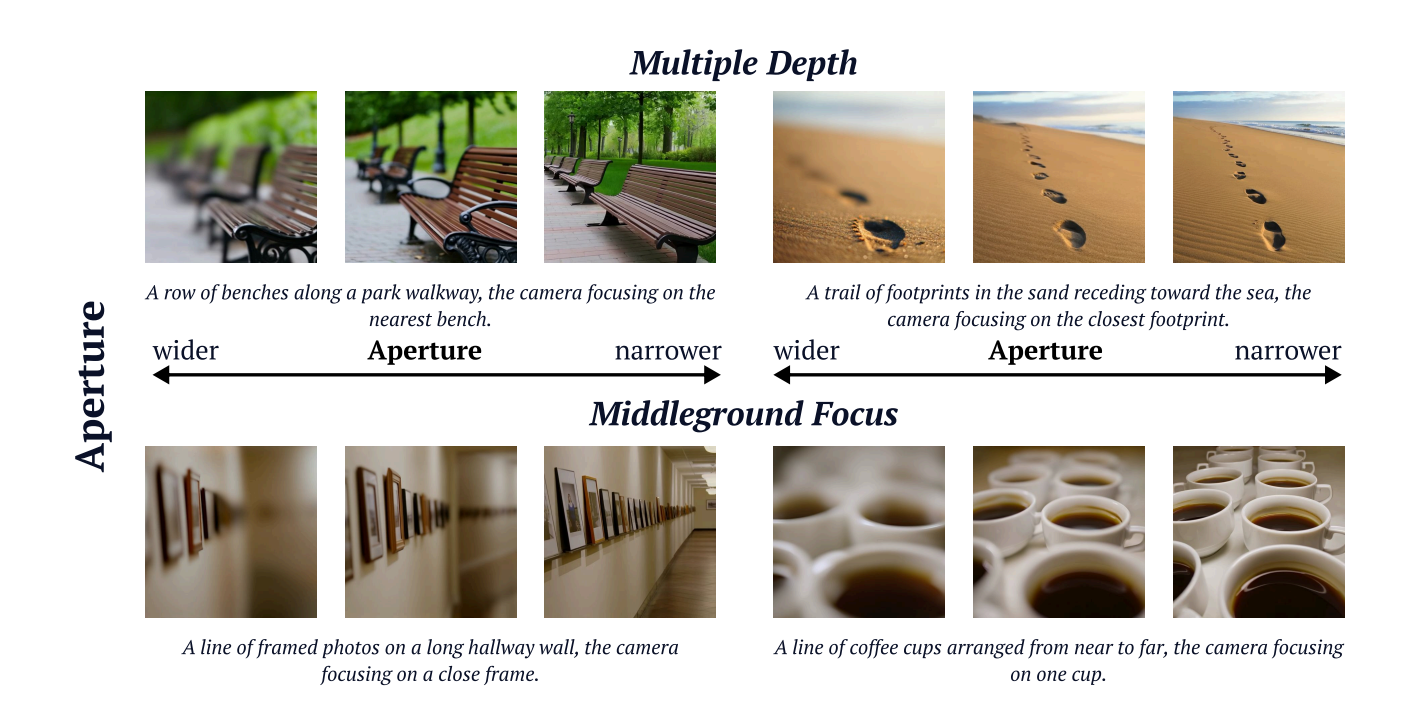
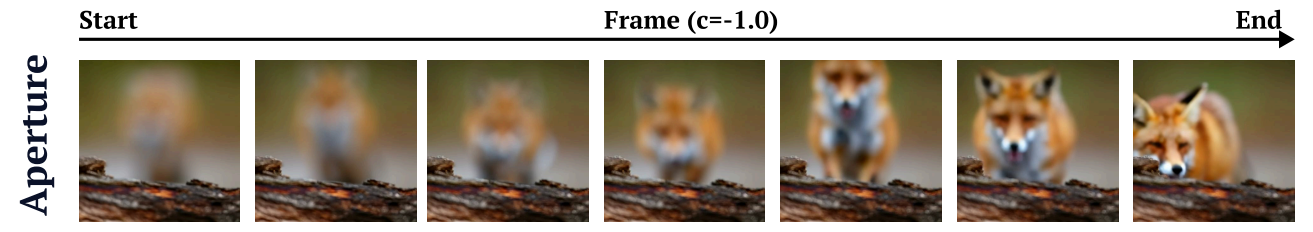


Figure 15. **Generalization of aperture control across diverse depth layouts and focal targets.** The model handles scenes with multiple depth layers and varied spatial arrangements, and can focus on locations beyond the foreground (e.g., mid- or background planes).



A fox running toward the camera and clearing a log in the foreground, the camera focusing on the log.

Figure 16. Despite being trained only on images, the model renders smooth bokeh variation as depth changes, enabled by the backbone's strong prior.

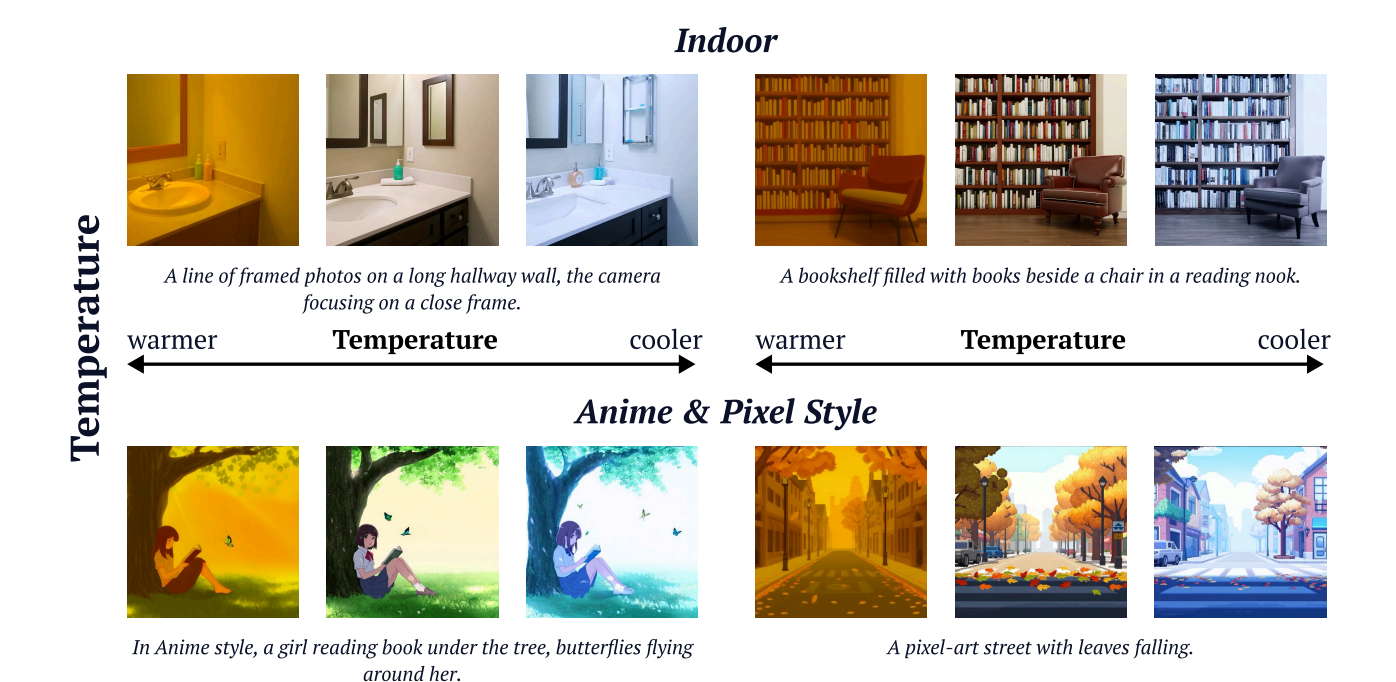


Figure 17. **Generalization of temperature control across a wide range of scene types.** The model produces stable cooler-to-warmer transitions in indoor environments as well as highly stylized domains such as anime and pixel art.